53-28-16

NACA

RESEARCH MEMORANDUM

CHARACTERISTICS OF FOUR NOSE INLETS AS MEASURED

AT MACH NUMBERS BETWEEN 1.4 AND 2.0

By George B. Brajnikoff and Arthur W. Rogers

Ames Aeronautical Laboratory
Moffett Field, Calif.

:s. . .on . .ac . . o (. . rt ng.a to Unclassified)

By . .the . . Nasa Tech Pub Announament T #98
(ER AUTHORIZED TO CHANGE)

By . . . . 24 Man 56.

GRADE OF OFFICER MAKING CHANGE)

7 Apr 61

NATIONAL ADVISORY COMMITTEE
FOR AERONAUTICS
WASHINGTON
June 25, 1951

319.98/13

NATIONAL ADVISORY COMMITTEE FOR AERONAUTICS

RESEARCH MEMORANDUM

CHARACTERISTICS OF FOUR NOSE INLETS AS MEASURED

AT MACH NUMBERS BETWEEN 1.4 AND 2.0

By George B. Brajnikoff and Arthur W. Rogers

SUMMARY

The pressure recovery, mass flow, and axial force of four bodies with nose inlets were measured at Mach numbers between 1.4 and 2.0 and angles of attack of 0°, 3°, 6°, and 9°. The Reynolds number based on the model inlet diameters varied between 0.4 and 0.8 million. Schlieren photographs of models at 0° angle of attack were used for calculation of the external wave drag resulting from the bow shock waves.

The drag coefficients of axially symmetric diffusers operating at the maximum mass-flow rates were calculated from schlieren photographs of the head shock waves and frictional drag considerations. The calculations showed good agreement with the measured values. At reduced mass-flow ratios the agreement was only fair. The results also show that the external drag of axially symmetric ducted bodies at 0° angle of attack can be predicted to a good degree of accuracy from theoretical considerations alone, if the entrance flow is supersonic and the point of transition of the boundary layer is known.

In general, it was found that the minimum axial-force coefficient occurred with maximum mass flow through the diffuser, and a small reduction in the mass flow resulted in a large increase in the axial-force coefficient. At reduced mass flows the effect of mass flow on the total-pressure recovery of a diffuser with a subsonic or a supersonic entrance was small. Changes in the angle of attack from 0° to 9° generally caused small decreases in the total-pressure recovery. In all cases when the maximum mass-flow decreased with increasing angle of attack the minimum axial-force coefficient increased by a considerable amount.

INTRODUCTION

The total drag of a supersonic aircraft propelled by a turbojet or a ramjet engine may be increased appreciably by an improperly designed induction system, particularly in view of the large size of the required air inlet in relation to the fuselage. Simultaneously, a low efficiency of the system in recovering the ram pressure reduces the thrust available from the engine. To avoid such consequences, a designer must be able to estimate the characteristics of inlet configurations likely to satisfy his design requirements.

For the cases of entirely supersonic flow around axially symmetric cowlings the external pressure or wave drag due to inlets can be determined theoretically (references 1 and 2). When such inlets operate at a reduced mass flow, a transonic flow region exists around the lip of the inlet and an entirely theoretical solution becomes extremely difficult. In such cases it is most practical to resort to experimental measurements of the drag force or to shadowgraph or schlieren pictures. Once the shape and location of the bow wave are known, it is possible to determine the pressure drag by the methods of references 3 and 4. A fair estimate of the frictional drag of a cowling at supersonic Mach numbers may be obtained through application of the present theories for various types of boundary layers (references 5 to 8), provided that the location of the transition region is known and there are no strong adverse pressure fields acting on the boundary layer. The pressure recovery at supersonic speeds can be estimated in cases of two-dimensional or axially symmetric inlets receiving little or no boundary layer by the methods of reference 9.

Four axially symmetric nose inlets have been tested in the Ames 8-by 8-inch supersonic wind tunnel in order to provide a basis for comparison with scoop inlets. It is the purpose of this report to present the characteristics of these nose inlets as determined by force and pressure measurements and to compare them with values calculated by various methods. Since forces were measured in the direction of the model axis only, the axial-force coefficients are presented instead of drag coefficients. Although axial and drag coefficients are synonymous only at zero angle of attack, drag symbols were used for axial forces for the sake of simplicity.

SYMBOLS

A area, square feet

a speed of sound, feet per second

C_a additive drag coefficient (due to diffusion ahead of entrance), dimensionless

C_D fore-drag coefficient $\left(\dfrac{D_F}{q_o A_{ref}}\right)$, dimensionless

C_{D_e} external axial-force coefficient measured along model axis $\left(\dfrac{D_e}{q_o A_{ref}}\right)$, dimensionless

C_{D_w} wave-drag coefficient $\left(\dfrac{D_e - D_f}{q_o A_{ref}}\right)$, dimensionless

D_e external force acting along model axis (does not include internal flow drag or base drag), pounds

D_F force acting along model axis (does not include base drag), pounds

D_f force acting along model axis due to friction on external model surface, pounds

d inlet diameter of cowling, feet

H total pressure, pounds per square foot

H_3 average total pressure at survey station weighted on area basis, pounds per square foot

l length of subsonic diffuser, feet

M Mach number $\left(\dfrac{V}{a}\right)$, dimensionless

m mass-flow rate $(\rho V A)$, slugs per second

m_1/m_o mass-flow ratio (ratio of mass flowing through the diffuser to that flowing in the free stream through an area equal to that of the flow area at the inlet station, $\dfrac{\rho_1 V_1 A_1}{\rho_o V_o A_1}$), dimensionless

P static-pressure coefficient $\left(\dfrac{p - p_o}{q_o}\right)$, dimensionless

p static pressure, pounds per square foot

q dynamic pressure $\left(\dfrac{1}{2}\rho V^2\right)$, pounds per square foot

R body ordinate, inches

Re   Reynolds number $\left(\dfrac{Vd}{\nu}\right)$, dimensionless

V   velocity, feet per second

x   distance from inlet station along model axis, feet

α angle of attack, degrees

γ ratio of specific heats for air = 1.40, dimensionless

ν kinematic viscosity, feet squared per second

ρ mass density, slugs per cubic foot

Subscripts

o   free stream

1   inlet station

2   diffuser exit

3   settling chamber (rake station)

4   outlet station (choked flow)

base   plane surface normal to model axis and constituting the rear boundary of the model

ref   reference area (frontal area of body exposed to stream), square feet

APPARATUS

Wind—Tunnel and Drag Balance

The tests of this investigation were performed in the Ames 8— by 8—inch supersonic wind tunnel in the range of Mach numbers between 1.40 and 2.01. The Reynolds number per foot of length was approximately 8 million at the lowest Mach number and 11 million at the highest. A detailed description of the tunnel and its auxiliary equipment is presented in reference 10.

Figure 1 shows the apparatus used to obtain simultaneous measure-
ments of the axial force, mass flow, and the pressure recovery of super-
sonic diffusers. As shown, a model is mounted on a steel shell that
floats on three rows of bearing balls inside a stationary shell sup-
ported by two struts. The fore and aft motion of the inner shell is
restricted only by the strain gage used for measuring axial forces.
Shrouds having somewhat smaller forward diameters than the bases of
models provide fairing between the bases of the models and the outer
shell. The shrouds and the stationary shell have orifices for measuring
static pressures acting on the base of the model and the ends of the
floating shell so that corrections for these pressures being other than
the free-stream static pressure can be made. Inside the inner shell,
which serves as a settling chamber, is a survey rake consisting of four
total and three static pressure tubes; this rake can be rotated from
outside the wind tunnel through 360° by means of a gear drive. The mass
flow through the model is controlled by a variable area outlet consist-
ing of a stationary ring and an adjustable plug operated by a wedge-
drive system. The ring is mounted rigidly on the survey-rake shaft so
that there is a clearance of 0.005 inch between its outer periphery and
the inner shell. Though such an arrangement does not allow reduction of
mass flow to zero, it provides a means for varying the flow rate without
exerting additional pressure forces on the inner shell. Measurements
with a model at angles to the stream direction can be made at angles of
3°, 6°, and 9° by attaching the balance at the proper angle in relation
to the horizontal strut as shown in figure 1.

MODEL DESCRIPTION

Figure 2 shows the models tested and gives their pertinent dimen-
sions. The first model, which was used to determine the accuracy of
force measurement, was a cone of 20° included angle; it had eight ori-
fices which were used to obtain the pressures acting on the surface of
the cone at the time of the drag-force measurement at 0° angle of attack.
The two open-nose inlet models, designated A and B, had the same external
shape. The entrance section of model A was cylindrical for a length of
1.5 diameters and was followed by a diffuser of constant divergence
angle. Model B had a contracting entrance designed so that supersonic
flow through the inlet could be established at $M_0=1.60$, according to the
relations for an inviscid, one-dimensional flow. The contraction was
followed by a short constant-area section, the purpose of which was to
stabilize a swallowed normal shock wave. This section was located so
that at a free stream Mach number of 1.70 the oblique conical-shock wave
from the cowling lip would be neutralized, if the flow were two-
dimensional, by the expansion wave originating at the forward end of the
straight section. Subsonic diffusion was accomplished by a passage of
constant divergence angle.

Model C was a conical-shock diffuser designed to handle approx-
imately the same mass of air per second at a Mach number of 2.01 as the
open-nose diffuser A at its maximum flow-rate condition. Model C had a
25°-semiangle cone and a cowling with a rounded lip located so that a
line joining the apex of the cone and the leading edge of the cowl made
a 45° angle with the model axis. The variation of the diffuser-area
ratio normal to the mean-flow direction is shown in figure 3. At the
design Mach number of 1.8 the diffuser was to operate with an external
normal shock wave. This model was about one-eighth the size of and
similar to a conical-shock diffuser tested at the NACA Lewis Laboratory
in the 8- by 6-foot supersonic wind tunnel.

Model D had a 30°-semiangle cone and a cowling with a sharp lip
located on a line originating at the apex of the cone and making a 46°
angle with the model axis. The maximum frontal areas of models C and D
were the same, but model D was designed to handle approximately 0.7 of
the mass flow of model C in the test range of Mach numbers. The external
surface area and length of cowling D were 55 and 62.6 percent of those
of model C, respectively, and model D had steeper angles between the
external surface and the model axis. The 20° cone, the central bodies
(inlet cones), and the cowlings were highly polished to ensure the long-
est run of laminar boundary layer possible under the existing test
conditions.

TEST METHODS

Instrumentation

The tunnel total pressure, the survey-rake pressures, and the base
pressures were measured on a multiple-tube mercury manometer. Dibutyl
phthalate was used to measure the differences between total and static
pressures registered by the survey rake at low-mass flow rates. The
total temperature of the flow and the temperature of the strain gage
(used for correcting the gage readings for thermal shift) were measured
by thermocouples registering the temperature on an indicating potentiom-
eter. Measurements of the axial force acting on the strain gage were
obtained in terms of deflection of a dynamically balanced galvanometer
calibrated for the gage in use. The flow about the model was observed
and photographed through a schlieren apparatus having a knife edge par-
allel to the direction of the free stream.

Procedure

The wind tunnel was calibrated with the aid of a rake of five
static-pressure probes to determine the static-pressure gradients

existing in the test section at the nominal Mach number settings of
1.40, 1.50, 1.70, 1.90, and 2.01. During the calibration and the sub-
sequent tests, the tunnel total pressure was maintained by manual con-
trol within ±0.1 inch of mercury of the preassigned value. In general,
the test procedure was similar to that of reference 10.

The number of pressure and force readings at a fixed mass-flow rate
and different angular positions of the survey rake varied from 5 to 10,
depending on the uniformity of the total-pressure distribution in the
diffuser. The pressure recovery and the axial force were measured for
six mass-flow ratios at a given Mach number and angle of attack; the
mass-flow settings were decided upon during the test after a preliminary
observation of the rate of axial force and pressure-recovery variation
with the outlet-area changes.

Reduction of Data

The total-pressure ratio H_3/H_0, as shown on the graphs, is based
on a value of pitot pressure weighted according to area. This average
value of H_3/H_0 was used in all calculations involving total pressure.

The mass-flow ratio was calculated from the following relation:

$$\frac{m_1}{m_0} = C \left(\frac{H_3}{H_0}\right) \frac{A_4}{A_1} \frac{1}{M_0} \left(\frac{2}{\gamma+1} + \frac{\gamma-1}{\gamma+1} M_0^2\right)^{\frac{\gamma+1}{2(\gamma-1)}}$$

This equation was derived on the assumption that the flow was inviscid
and one-dimensional in nature; with the exception of a correction factor
C, this relation is identical to that given in reference 10. This fac-
tor was obtained by testing open-nose inlets of various inlet diameters
operating with swallowed head shock waves. The factor C was found to
be independent of small changes in the velocity profile at the survey-
rake station.

The external axial force was determined by subtracting from the
force measured by the balance the sum of the forces due to (1) the
change of momentum and static pressure of the internal flow from the free
stream to the rake station, (2) the base drag, and (3) the force due to
buoyancy. The base drag forces were caused by pressures other than the
free-stream static pressure acting on the base of the model and the
floating shell. The buoyancy force was considered to equal the inte-
grated product of the local increment in the tunnel static pressure
(existing between the local and the reference stations in the absence of
a model) and the local differential element of external surface area
normal to the model axis. Since the force normal to the model axis was
not measured, only the axial-force coefficients are presented. At 0°

angle of attack the external axial—force coefficients are equal to the
external drag coefficients which include the cowl drag and drag due to
diffusion ahead of the duct entrance.

Accuracy of Results

The accuracy of the test results depended principally on the time
correlation as well as the precision of the pressure and force measure—
ments since in many cases the flow through the model was unsteady.
Although the force readings and the photographs of the manometer board
were taken simultaneously, the difference in response of the measuring
apparatus to changes in the measured quantities introduced errors of
magnitudes determined by the frequency and the amplitude of the vari—
ation. The inaccuracies due to the various causes, together with their
maximum cumulative magnitudes estimated in terms of the external axial—
force coefficient of the model tested, are tabulated as follows:

I. Steady—flow conditions (very small and slow variation in H_o)

    A. 20° cone

        Source of error: $\pm\Delta C_{D_e}$

        1. Manometer precision and lag................... 0.002
        2. Balance friction............................. .001
            Maximum cumulative total................... 0.003

    B. Diffusers

        Source of error: $\pm\Delta C_{D_e}$

        1. Manometer precision and lag................... 0.002
        2. Balance friction............................. .003
        3. Internal flow momentum estimate[1]........... .003
            Maximum cumulative total................... 0.008

II. At unsteady flow conditions the accuracy of axial—force measure—
    ments was poor.

Figure 4 shows the results of force measurements made with a 10°—
semiangle cone set at 0° angle of attack. This figure also shows the
theoretically predicted values of the shock—wave, or pressure, drag taken
directly from the tables of reference 11 and the frictional drag as
estimated on the basis of the low—speed skin—friction coefficients given

---

[1]The mass—flow ratio estimates are believed correct to ± 1—1/2 percent.

in reference 5, corrected for compressibility by the method of reference
8, and modified for the three-dimensional flow effect as suggested in
reference 12. All the turbulent skin-friction coefficients were cor-
rected for compressibility using the properties of air at the model sur-
face as suggested in reference 7. It is evident that the experimental
and theoretical pressure-drag coefficients agreed very well, and that
the total fore drag of the cone as measured by the balance also agreed
within the expected accuracy with the predicted values of total drag
based on the assumption that the boundary layer on the model was laminar.
The repeatability and consistency of the results of drag-force measure-
ments indicate that the drag balance performed satisfactorily.

RESULTS AND DISCUSSION

Open-Nose Diffusers

The variation of the total-pressure ratio and the external axial-
force coefficient with mass-flow ratio of model A is shown in figure 5
for 0° angle of attack at three free-stream Mach numbers. With super-
sonic flow through the inlet $(m_1/m_0=1.0)$, the maximum total-pressure
ratios in the settling chamber of model A were 0.93 to 0.95 of the theo-
retical recovery through a normal shock wave. Large transverse pressure
gradients as a result of transitory separation of flow occurred in the
diffuser when the area ratio between the exit and the inlet was increased
more than necessary for the entrance of the normal shock wave into the
inlet. This condition was manifested by the large erratic variations in
the readings of the survey rake and was responsible for considerable
scatter of the force data at large area ratios.

The external axial-force coefficient of model A increased rapidly at
all Mach numbers with the emergence of the normal shock to a position
ahead of the inlet; as the mass-flow ratio was reduced to 0.9 from 1.0,
the coefficient approximately doubled in magnitude. Unfortunately, the
wave drag of models A and B operating at mass-flow ratios below 1.0 could
not be calculated from the schlieren pictures because the photographs did
not cover a sufficiently large part of the head wave (see appendix).

At mass-flow ratios less than the maximum, the portion of the drag
due to diffusion (the additive drag) can be obtained by the method of
reference 13. This additive drag is accompanied by a change in the pres-
sures on the external surface of the diffuser (reference 14). In the
present tests, these pressures were not measured and the theoretical
additive drag coefficients were simply added to the minimum drag coef-
ficients. Thus, the difference between the measured and the estimated
drag-rise curves is the result of neglecting the change in pressure on
the cowling, of experimental and theoretical inaccuracies, and possibly

of a change in the location of the boundary-layer transition region. However, figure 5 shows that the major portion of the drag rise can be predicted even if these factors are ignored.

Figure 6 shows the total-pressure ratio and the external axial-force-coefficient variation with mass-flow ratio, angle of attack, and Mach number for model B. The maximum mass-flow ratio at the Mach number of 1.4 was only 0.97 because the contraction of the entrance section was too great to permit the normal shock wave to enter the inlet at that speed or to remain inside the diffuser at $M_0 = 1.4$ after entry at a higher Mach number. The total-pressure ratio and the axial-force coefficient of model B at the Mach number of 1.4 were nearly the same as those of model A for equal mass-flow ratios. At a Mach number of 1.7 and higher, the head shock wave entered the inlet. Its position depended entirely on the static pressure in the settling chamber of the model, and a hysteretic variation of the total-pressure ratio with the mass-flow ratio was observed. This is indicated in figure 6 by a peak in the pressure-recovery curves at $m_1/m_0 = 1.0$. The maximum total-pressure ratios of model B were 0.02 to 0.04 higher than those of model A or approximately 0.95 to 0.98 of recovery through a normal shock wave. At equal mass-flow ratios the external axial-force coefficients of models A and B were nearly the same.

The effects of the angle of attack on the characteristics of model B, as shown in figure 6, were generally small. The external axial-force coefficient seemed to increase with an increase in the angle, but the data were inconclusive because the magnitudes of the measured effects were comparable to experimental scatter.

Figure 7 shows the variation of the minimum external axial-force coefficients of models A and B with Mach number at 0° angle of attack; it also presents the values of the pressure drag, as predicted by the method of reference 1, and the laminar and turbulent friction drag calculated from the low-speed skin-friction coefficients of reference 5. A compressibility correction to the turbulent skin-friction coefficients has been applied as suggested in reference 7, using the properties of air at the cowling surface. The laminar friction coefficients were corrected for compressibility using the method of reference 8. The calculations were made on the assumption that the frictional force on the external surface of each model (A and B) was equal to that on a flat plate of length and area equal to those of the cowlings.

The minimum external axial-force coefficients of model A show good agreement with the predicted values of drag coefficients at all Mach numbers except 2.01. A plausible explanation for the high value of the experimental coefficient at $M_0 = 2.01$ is provided by the schlieren photographs of figure 8. A mild pressure disturbance may be seen originating

on the model at a station located approximately 0.4 of the model length from the entrance at the higher Mach number. Since this phenomenon existed only at the highest Reynolds number, it is reasonable to assume that it was caused by boundary-layer transition.[2] The drag coefficient calculated on the assumption of laminar boundary layer existing on the model up to 40 percent of the cowl length, and fully turbulent layer from there on, agrees fairly well with the measured value. (See fig. 7.) Better agreement would be obtained if the additional wave drag due to the pressure disturbance were not neglected. It should be noted that the Reynolds number based on the length of the laminar portion of the boundary layer is quite low for natural transition (Re=1.14 million).

As shown in figure 7, the minimum external axial-force coefficient of model B at a Mach number of 1.4 was almost one and one-half times that of model A. The increase apparently was due to the spillage around the cowling lip caused by the external normal shock wave. At a Mach number of 1.5, the higher value of the minimum axial-force coefficient prevailed when overspeeding (approaching the test Mach number from a higher value) was not used to establish supersonic flow through the inlet. The lower coefficient was obtained for the diffuser when the entrance velocity was supersonic. At Mach numbers in excess of 1.5 the head shock wave entered the diffuser without overspeeding, and the minimum axial-force coefficients of model B were comparable to those of model A. Schlieren photographs of model B reveal that at the free-stream Mach number of 2.01 transition of the boundary layer appears to have occurred at the same location as that of model A and apparently caused a similar increase in the measured axial-force coefficient.

Conical-Shock Diffusers

The characteristics of model C are shown in figure 9. It was found necessary to increase the lowest test Mach number to 1.5 in order to avoid choking the tunnel when the model was set at 9° angle of attack; however, no difficulty was encountered at $M_0=1.4$ for $\alpha=0^\circ$.

The general characteristics of flow through model C were similar to those through the open-nose diffusers with the exception that a region of flow instability was encountered when the mass-flow ratio of model C was reduced below about three-quarters of the maximum possible at the given Mach number. This condition was caused possibly by the interaction

---

[2]Unpublished data of tests conducted in the NACA Ames 1- by 3-foot supersonic wind tunnel and the supersonic free-flight tunnel show that mild pressure waves are generated by the boundary layer undergoing natural transition.

between the boundary layer and the shock waves on the cone and the back
pressure in the subsonic diffuser (see reference 10), or by internal
flow separation at the cowling wall resulting from the entrance of a
velocity discontinuity sheet as suggested in reference 15.

The total—pressure recovery at the Mach number of 1.50 was 0.95 of
that through a normal shock wave; at $M_O=2.01$ it was 10 percent higher
than the normal wave recovery. The maximum total pressure measured in
the settling chamber of this model at $M_O=1.90$ was only 3 percent less
than that of the similar model tested at the Lewis Laboratory ($M_O=1.85$)
at Reynolds numbers four and one—half times that of model C. These
maxima occurred at the same mass—flow ratio.[8]

The values of the external axial—force coefficient at 0° angle of
attack of model C were about one and a half to two times those of
model A, probably because of the additive drag due to diffusion ahead
of the entrance, as discussed in reference 13. Figure 9 also shows the
external drag coefficients calculated from the schlieren photographs by
the method of reference 3, using an approximation suggested by Nucci of
the Langley Laboratory to estimate the drag due to the outer portion of
the bow shock wave. (See reference 16 or appendix.) The values shown
were calculated using $K=1.0$ and include the drag due to laminar
friction calculated on the basis of low—speed skin—friction coefficients
(reference 5) corrected for compressibility (reference 8).

In general, the assumption of laminar boundary—layer flow resulted
in a fair estimate of the external drag (axial—force coefficient at
$\alpha=0^O$) through the range of test Mach numbers at maximum mass—flow ratios.
The drag coefficients, as calculated from wave photographs, of the inlet
operating at a reduced mass flow were low in all cases. The discrepancy
is probably due to the inaccuracy of calculation caused by insufficient
length of the head shock wave visible in the photographs, as discussed
in the appendix. At a Mach number of 2.01, where transition of the
boundary layer is most likely to occur (see discussion of models A and
B), and at a reduced mass—flow ratio the difference in drag coefficients
amounts to that which would be caused by transition at 0.6 of the
cowling length. (See fig. 9(c).) The sum of the minimum external axial—
force coefficient and the additive drag coefficient, as calculated using
reference 13, is also shown in figure 9. This approximation apparently
gives a fair estimate of the external axial—force coefficient at
moderately reduced mass—flow ratios.

---

[3] Since the mass—flow ratios as used by the Lewis Laboratory are based on
the area fixed by the inlet diameter and not flow area, the numerical
values of m_1/m_O are not identical unless adjusted to a common refer—
ence area.

The minimum external axial—force coefficient of model C, as shown
in figure 10, increased from 0.047 at the Mach number of 1.4 to 0.097
at $M_O=1.7$ and then decreased to 0.083 at $M_O=2.01$. This trend is con—
sistent with that stated in reference 13 for the additive drag (which
constitutes the major portion of wave drag) when the observations listed
below are considered:

1. At the Mach numbers below 1.9, the normal shock wave remained
outside the inlet at all mass—flow ratios.

2. At and above a Mach number of 1.9, the normal shock wave was
inside the inlet at the maximum flow condition.

Figure 10 also shows the minimum external—drag or axial—force coef—
ficients at $\alpha=0^O$ of the model tested at the Lewis Laboratory. It is
evident that a fair agreement exists between the values of external wave
drag coefficients of the two models after the frictional drag was sub—
tracted. (See fig. 10.) The discrepancies may be due to the experi—
mental inaccuracies and due to probable slight differences in the lip
radii of the two cowlings. Because of the small size of model C, a
small error in the lip shape due to machining may be responsible for a
large portion of the observed difference in the minimum wave—drag coef—
ficients at $M_O=2.01$. The effects of lip shape are greatest when the
shape affects the position of the entrance shock wave as is the case at
maximum mass—flow ratios when the free—stream Mach number is sufficiently
high.

Variations in the angle of attack (see fig. 9) showed small effects
on the characteristics of model C at lower Mach numbers. It should be
noted that in this case the maximum mass—flow ratio was not affected
appreciably. However, when the mass—flow ratio decreased 5 percent for
$\alpha=9^O$ at $M_O=2.01$, the total—pressure ratio decreased approximately 6
percent and the minimum axial—force coefficient increased about 60 per—
cent.

The characteristics of model D are presented in figure 11. The max—
imum mass—flow ratio of this model was larger than that of model C
because of a larger cone angle, a larger angle between the model axis
and the line joining the cone apex and the leading edge of the cowl, and
a sharp lip. The total—pressure ratios of models D and C were nearly the
same at the lower Mach numbers; at $M_O=2.01$ the maximum recovery of
model D was about 5 percent greater.

The drag coefficients calculated from schlieren photographs using
the same methods as those used in the case of model C also are shown in
figure 11. At large mass flows the calculated drag coefficients are in
fair agreement with the measured values. At all Mach numbers the

photographs showed a smaller portion of the head shock wave than with model C, and thus the calculated values of drag were subject to greater error. The drag coefficient (minimum plus additive) as calculated using reference 13 seems to give a fair estimate of axial—force coefficient at reduced mass—flow ratios.

The effects of angle of attack on the performance of model D were large throughout the range of test Mach numbers. The largest effects on the minimum axial—force coefficient were observed at $M_O=2.01$. For an angle of attack change from 0° to 9°, the maximum mass—flow ratio decreased about 8 percent and caused the minimum force coefficient to increase approximately 20 percent and the maximum total—pressure ratio to decrease 8 percent. The reason for the large difference in the exter—nal axial—force coefficients at reduced mass—flow ratios (see $M_O=1.70$ curve, fig. 11) is not clearly evident.

The variation of the minimum external axial—force coefficient of model D with the Mach number is shown in figure 12. The trend is similar to that of model C.

In comparing the axial—force coefficients of the various models, consideration should be given to the effects of boundary—layer transi—tion. Transition, as indicated by schlieren photographs, is known to have occurred on models A and B at certain test conditions. However, this method of detecting transition is not extremely sensitive and there—fore it is possible that transition could have occurred on the rear por—tion of any of the models tested without being detected. Since the frictional drag constituted a significant portion of the measured axial force, a change in location of transition would have had a pronounced effect on the measured force. The frictional drag was not measured directly and, therefore, the shown variations of the external axial—force coefficients with mass—flow ratio include the effects of changes in the boundary layer. This fact may be responsible for at least part of the difference between the measured values of external axial—force coefficient at reduced mass—flow ratios and those calculated from schlieren photographs, since the boundary layer was assumed to be laminar.

CONCLUSIONS

The performance characteristics of four nose inlets were measured in the NACA Ames 8— by 8—inch supersonic wind tunnel at Reynolds numbers between 0.4 and 0.8 million based on the inlet diameters. The investi—gation was conducted in the range of Mach numbers between 1.40 and 2.01 and led to the following conclusions:

1. Good agreement was obtained between the measured external axial-force coefficients at 0° angle of attack and the calculated drag coefficients of diffusers operating at maximum mass-flow ratios. The values of minimum wave drag obtained for a conical-shock inlet showed fair agreement with those measured in the 8- by 6-foot supersonic tunnel at the NACA Lewis Laboratory using a similar model at Reynolds numbers four and one-half times larger.

2. The external axial-force coefficients of the conical-shock inlets using all-external supersonic compression were about one and a half to two times those of the open-nose inlets with supersonic entrances.

3. Minimum external axial-force coefficients occurred at maximum mass-flow ratios and small reductions in the mass-flow ratios considerably increased the external axial-force coefficients of all the inlets.

4. The sum of the minimum external axial-force coefficients and the theoretical additive-drag coefficients gave a fair estimate of drag coefficients of inlets tested at reduced mass-flow ratios.

5. The effects of angles of attack on the pressure recovery were generally small. The external axial-force coefficients increased measurably with the angle of attack only in cases where the maximum mass-flow ratio decreased with increasing angle.

Ames Aeronautical Laboratory,
     National Advisory Committee for Aeronautics,
          Moffett Field, Calif.

APPENDIX

EVALUATION OF DRAG OF AXIALLY SYMMETRIC BODIES

FROM SHOCK-WAVE PHOTOGRAPHS

When the speed of the flow around a body changes from a supersonic velocity in the free stream to a subsonic velocity and then accelerates to a supersonic speed again, the mathematical equations that describe the flow behavior change in nature from hyperbolic to elliptic and back to hyperbolic. Since no known analytical methods exist for simultaneously solving hyperbolic and elliptic differential equations with incomplete boundary conditions, a laborious method of matching individual solutions must be used. If a photograph of the bow wave ahead of an axially symmetric body at 0° angle of attack is available, the wave drag can be determined through use of any of the following three methods:

1. Integration of the momentum and pressure change between two infinite control planes as in figure 13

2. Integration of the entropy rise across the bow shock wave

3. Integration of the momentum and pressure change within a closed flow region adjacent to the body, the conditions within this region being calculated by the method of characteristics

These three methods have been proposed in the references cited below. It is the purpose of this appendix to review and further clarify the procedures involved by presenting derivations and detailed comments not given previously.

The first two methods require knowledge of the shape of the wave out to the point where its strength is zero, while the third method requires only the portion of the wave bounding the characteristics net ending at the rear of the body. Since in practice the entire wave cannot be photographed due to physical limitations, an approximation must be used to account for the drag contribution of the unavailable portion of the wave in the first two methods; thus the accuracy depends on the exactness with which the decay of the bow wave may be predicted.

Method 1: This method was proposed and used in reference 3. A schematic drawing of a body and its head shock wave is shown in figure 13. The body is assumed to have a blunt nose followed by an infinitely long cylindrical afterbody, so that, neglecting friction, the entire body drag appears in the detached bow wave. Considering the control

surface s shown in figure 13, one can write the following steady-flow equation for the summation of forces in the x direction on the control surface:

$$\int_s \int [\rho u V_n + p \cos(n,x)] \, ds = 0 \tag{A1}$$

where

V_n velocity compoent normal to the control surface

$p \cos(n,x)$ pressure component in the x direction

u local velocity component in the x direction

n outward normal to s

With reference to figure 13, equation (A1) may be rewritten as

$$\int_0^\infty (-\rho_0 u_0{}^2 - p_0) \, 2\pi y \, dy + \int_r^\infty (\rho u^2 + p_0) \, 2\pi \eta \, d\eta +$$

$$(\text{drag measured from } p=0) = 0$$

or

$$-2\pi \int_0^\infty (\rho_0 u_0{}^2 + p_0) \, y \, dy + 2\pi \int_r^\infty (\rho u^2 + p_0) \, \eta \, d\eta +$$

$$\int_0^r (p - p_0) \, 2\pi r_1 \, dr_1 + \int_0^r p_0 \, 2\pi r_1 \, dr_1 = 0$$

where

p local pressure on the body

Since the third integral is the body drag relative to the free-stream static pressure, the last equation may be solved for drag.

$$D_W = 2\pi \int_0^\infty (\rho_0 u_0{}^2 + p_0) \, y \, dy - 2\pi \int_r^\infty (\rho u^2 + p_0) \, \eta \, d\eta - p_0 \pi r^2$$

The second integral may be replaced by the difference of two integrals,
the first extending from zero to infinity and the second from zero to r.
Thus one obtains

$$D_W = 2\pi \int_0^\infty (\rho_0 u_0^2 y\,dy - \rho u^2 \eta\,d\eta)$$

When the continuity relation between the two control surfaces

$$2\pi\rho_0 u_0 y\,dy = 2\pi\rho u \eta\,d\eta$$

is applied, the drag equation becomes

$$D_W = 2\pi\rho_0 u_0^2 \int_0^\infty \left(1 - \frac{u}{u_0}\right) y\,dy$$

and the drag coefficient is given by

$$C_{D_W} = \frac{D_W}{q_0 A} = \frac{2D_W}{\rho_0 u_0^2 \pi r^2} = 4 \int_0^\infty \left(1 - \frac{u}{u_0}\right) \frac{y}{r}\,d\left(\frac{y}{r}\right) \qquad (A2)$$

By means of the energy equation

$$(u/u_0)^2 = 1 + \left[2/(\gamma-1)M_0^2\right]\left[1 - (T/T_0)\right]$$

and the entropy relation

$$\Delta s = c_p \ln \frac{T}{T_0} - R \ln \frac{p}{p_0}$$

(where T/T_0 and p/p_0 are static temperature and pressure ratios,
respectively, across the head shock wave)

or

$$\frac{T}{T_0} = e^{\frac{\Delta s}{c_p}} = \left(\frac{H_0}{H}\right)^{\frac{\gamma-1}{\gamma}} = \left[\frac{2\gamma M_0^2 \sin^2\theta - (\gamma-1)}{\gamma+1}\right]^{\frac{1}{\gamma}} \left[\frac{(\gamma-1)M_0^2\sin^2\theta + 2}{(\gamma+1)M_0^2\sin^2\theta}\right]$$

equation (A2) can be written as

$$C_{D_W} = 4\int_0^\infty \left[1 - \frac{\frac{y}{r}}{\sqrt{1 + \frac{2}{(\gamma-1)M_0^2}\left\{1 - \left[\frac{2\gamma M_0^2\sin^2\theta - (\gamma-1)}{\gamma+1}\right]^{\frac{1}{\gamma}}\left[\frac{(\gamma-1)M_0^2\sin^2\theta + 2}{(\gamma+1)M_0^2\sin^2\theta}\right]\right\}}}\right]\frac{y}{r}\,d\left(\frac{y}{r}\right)$$

$$(A3)$$

where θ is the local shock wave angle (see fig. 13), T_O and H_O are free stream total (stagnation) temperature and pressure, respectively, and T and H correspond to conditions immediately downstream of the wave.

From a photograph of the flow about a body at a known Mach number, the values of wave angle θ can be tabulated for corresponding (y/r) distances, and the drag obtained by graphical integration of equation (A3).

Method 2: The method of integration of the entropy rise across the bow shock wave was proposed in reference 17 (equation (68)), from which the following expression is readily obtained:

$$C_{D_W} = \frac{4}{\gamma M_O{}^2} \int_O^\infty \ln\left(\frac{H_O}{H}\right)\frac{y}{r}\, d\left(\frac{y}{r}\right) \tag{A4}$$

This equation can be transformed by use of the energy and entropy relations into

$$C_{D_W} = \frac{4}{\gamma M_O{}^2} \int_O^\infty \ln\left\{\left[\frac{2\gamma M_O{}^2 \sin^2\theta - (\gamma-1)}{\gamma+1}\right]^{\frac{1}{\gamma-1}}\right.$$
$$\left.\left[\frac{(\gamma-1)M_O{}^2 \sin^2\theta + 2}{(\gamma+1)M_O{}^2 \sin^2\theta}\right]^{\frac{\gamma}{\gamma-1}}\right\}\frac{y}{r}\, d\left(\frac{y}{r}\right) \tag{A5}$$

Equations (A3) and (A5) are equivalent expressions for the wave drag.

Method 3: The determination of the body surface pressure distribution by the method of characteristics has been explained and used in references 4 and 16. Although very laborious, this method requires a picture of the shock wave only extensive enough to complete the characteristics net to the body surface. With such a photograph, this method is more accurate than the first two.

Of the three methods, the first two have presupposed a picture of the entire shock wave, or at least that portion of the wave across which the entropy changes significantly. In practice, however, such an extensive picture of a shock wave is generally unobtainable. An approximation is therefore required to account for the drag contribution of the unavailable portion of the wave.

References 18 and 19 suggest a method for finding the pressure drag due to the portion of the head shock wave bordering the subsonic region at the nose of a blunt body. This method approximates the head shock

wave by a hyperbola asymptotic to a free-stream Mach wave. In order to determine if a close estimate of drag due to a complete head shock wave could be obtained through this method by extrapolation of the hyperbola to infinity, the head wave drag of a sphere at three Mach numbers was computed. The results shown in figure 14 indicate poor agreement with measurements of the actual fore drag of spheres. The discrepancy is probably due to the fact that a hyperbola approximates the shape of the shock wave well enough only in the section bordering the subsonic region, while the shape of the outer part of the shock wave depends largely on the shape of the body. Since in the case of a sphere the shock-wave curvature changes continuously, the use of a hyperbola to obtain the entire pressure drag seemed reasonable. The curvature of a shock wave produced by a diffuser with a subsonic entrance usually does not change continuously all along its length; therefore the application of a hyperbolic curve is invalid for determination of drag due to a complete wave.

An approximation, outlined in reference 16, is valuable since it obviates need for knowledge of the outermost portion of the wave or the construction of the characteristics net. Again referring to figure 13, for the flow through a control plane HA, within the streamtube bounded by the streamlines HGF and ABCDE, the continuity equation states

$$2\pi\rho_0 u_0 y \, dy = 2\pi\rho u \eta \, d\eta$$

or

$$\rho_0 u_0 \, d\left(y^2\right) = \rho u \, d\left(\eta^2\right)$$

therefore

$$\eta^2 = \int_0^{y^2} \left(\frac{\rho_0}{\rho}\right)\left(\frac{u_0}{u}\right) d\left(y^2\right) + r^2$$

(since $\eta = r$ when $y = 0$)

With u_0/u given above by the energy equation, and

$$\frac{\rho_0}{\rho} = \frac{T}{T_0} = \left(\frac{H_0}{H}\right)^{\frac{\gamma-1}{\gamma}}$$

it follows that

$$\eta^2 = \int_0^{y^2} \frac{\left(\dfrac{H_0}{H}\right)^{\frac{\gamma-1}{\gamma}}}{\sqrt{1 + \dfrac{2}{(\gamma-1)M_0^{\,2}}\left[1 - \left(\dfrac{H_0}{H}\right)^{\frac{\gamma-1}{\gamma}}\right]}}\, d\left(y^2\right) + r^2$$

or

$$\left(\frac{\eta}{r}\right)^2 - \left(\frac{y}{r}\right)^2 = \int_0^{\frac{y^2}{r^2}} \left\{ \frac{\left(\frac{H_o}{H}\right)^{\frac{\gamma-1}{\gamma}}}{\sqrt{1 + \frac{2}{(\gamma-1)M_o^2}\left[1 - \left(\frac{H_o}{H}\right)^{\frac{\gamma-1}{\gamma}}\right]}} - 1 \right\} d\left(\frac{y}{r}\right)^2 + 1 \tag{A6}$$

where

$$\left(\frac{H_o}{H}\right)^{\frac{\gamma-1}{\gamma}} = \left[\frac{2\gamma M_o^2 \sin^2\theta - (\gamma-1)}{\gamma+1}\right]^{\frac{1}{\gamma}} \left[\frac{(\gamma-1)M_o^2\sin^2\theta + 2}{(\gamma+1)M_o^2\sin^2\theta}\right]$$

Now, writing the summation of forces for the region HABCDEFGH, one obtains

$$c_{D_W} = \left(c_{D_W}\right)_o + \frac{p-p_o}{q_o}\left[\frac{\pi(\eta^2-y^2)}{\pi r^2}\right] = \left(c_{D_W}\right)_o + \frac{p-p_o}{\frac{1}{2}\gamma p_o M_o^2}\left[\left(\frac{\eta}{r}\right)^2 - \left(\frac{y}{r}\right)^2\right]$$

or

$$c_{D_W} = \left(c_{D_W}\right)_o + \frac{2(K-1)}{\gamma M_o^2}\left[\left(\frac{\eta}{r}\right)^2 - \left(\frac{y}{r}\right)^2\right] \tag{A7}$$

where

$$K = \left(\frac{p}{p_o}\right)_{GF}$$

where $\left(c_{D_W}\right)_o$ is the drag coefficient obtained by use of equation (A3) or (A5) for the region between B and G. Point G is assumed to be the last visible point on the shock-wave photograph, and K is the ratio of the static pressure at some point along the streamline from point G to point F to p_o.

The value of K is known only at the points G and F along the streamline, being given at point G by the equation for the pressure rise through an oblique shock wave

$$\left(\frac{p}{p_o}\right)_G = \left[\frac{2\gamma M_o^2\sin^2\theta - (\gamma-1)}{\gamma+1}\right]_G$$

and equal to unity at point F. Hence the average pressure ratio K
lies between $(p/p_o)_G$ and 1.0. The choice of $K = (p/p_o)_G$ generally
results in an overestimated drag coefficient, while the choice of
$K = \frac{1}{2}\left[1+(p/p_o)_G \right]$ generally yields an underestimated value of C_{D_w}.

The fraction of the total drag taken into account by the approximation
should be small if good accuracy is desirable. Thus the value of
$(C_{D_w})_o$ must be calculated for a maximum span of the bow wave for best
accuracy.

Before applying the above methods to the calculation of the drag of
diffusers, it was decided to test the procedure on spheres, for which an
experimental fore-drag curve and excellent wave photographs were avail-
able. Figure 14 shows the experimental data from reference 20 and the
calculated values of drag. It is evident that the portions of the head
shock waves contained in the photographs from which the wave drag was
calculated were insufficient for accurate determination of the drag
coefficients. Since the photographs showed the wave shapes up to 15
sphere radii from the axis of symmetry, it may be concluded that the
visible part of the wave must be definitely in excess of this figure.
The indicated differences between the drag coefficients calculated by
the momentum method (equation (A3)) and the entropy method (equation
(A5)) are due solely to inaccuracies in calculations and mechanical
integrations. The approximation outlined in reference 16, when applied
to the drag curve of figure 14 as calculated by the momentum method,
yields a much better estimate of the drag coefficients. However, to
obtain this agreement it was necessary to use for K the full value of
pressure ratio across the oblique shock wave at the extreme y/r visible
on the photograph.

Application of the method of characteristics, as outlined in refer-
ence 4, to the flow around a 1-inch-diameter sphere at a Mach number of
3, proved unsuccessful. The characteristics net could not be completed
from the shock wave to the sphere because of extremely slow convergence
of the Mach net toward the sphere. The schlieren photographs of spheres
used for drag calculations were taken in the Ames 1- by 3-foot supersonic
wind tunnels No. 1 and No. 2.

ADDITIONAL CONSIDERATIONS

The experience of calculating drag from wave photographs led to a
few observations which may aid in future work:

1. The photograph of the wave must be clear, accurate, and exten-
sive, in excess of 15 maximum body radii if possible. Shadowgraph

pictures are preferable to schlieren photographs because of better def-inition of the head-wave curvature near the leading edges of cowlings; a small error in the apparent curvature of the wave immediately adjacent to the lip of a cowling of small angle may result in a large error in the calculated drag.

2. The free-stream Mach number must be accurately known (for a sphere at $M_0 = 1.520 \pm 0.004$, $\Delta C_{D_w} = \pm 0.01$).

3. The position of the body should be such that the head wave it creates does not intersect any other pressure disturbances which may be present in the tunnel (e.g., shock or expansion waves created by tunnel-wall imperfections, model support, etc.).

4. The methods are not applicable to the calculation of drag of a body the cross-section of which continually increases within the field of view. In this case, a large portion of the drag would have to be estimated by means of the approximation suggested by Nucci, and the error in calculated drag coefficient would be large.

5. A body of revolution may yaw slightly without disturbing the symmetry of the detached head shock wave; consequently, the wave axis of symmetry rather than the body axis should be used as the x axis. The calculated drag coefficient must be resolved in such cases in the direction of the body axis to obtain the axial-force coefficient.

REFERENCES

1. Brown, Clinton E., and Parker, Hermon M.: A Method for the
   Calculation of External Lift, Moment, and Pressure Drag of
   Slender Open—Nose Bodies of Revolution at Supersonic Speeds.
   NACA Rep. 808, 1945.

2. Ferri, Antonio: Application of the Method of Characteristics to
   Supersonic Rotational Flow. NACA Rep. 841, 1946.

3. Munk, Max M., and Crown, J. Conrad: The Head Shock Wave. Naval
   Ord. Lab. Memo. No. 9773, Aug. 25, 1948.

4. Ferri, Antonio: Method for Evaluating from Shadow or Schlieren
   Photographs the Pressure Drag in Two—Dimensional or Axially
   Symmetrical Flow Phenomena with Detached Shock. NACA TN 1808,
   1949.

5. Prandtl, L.: The Mechanics of Viscous Fluids. Aerodynamic Theory,
   vol. III, by Durand, W. F., California Inst. of Technology,
   Pasadena, 1943.

6. Schlichting, H.: Lecture Series, "Boundary Layer Theory," Pt. I —
   Laminar Flows. NACA TM 1217, 1949. Pt. II — Turbulent Flows.
   NACA TM 1218, 1949.

7. Frankl, F., and Voishel, V.: Turbulent Friction in the Boundary
   Layer of a Flat Plate in a Two—Dimensional Compressible Flow at
   High Speeds. NACA TM 1053, 1943.

8. von Kármán, T., and Tsien, H. S.: Boundary Layer in Compressible
   Fluids. Jour. Aero. Sci., vol. 5, no. 6, 1938, p. 227.

9. Oswatitsch, K.: Pressure Recovery for Missiles With Reaction
   Propulsion at High Supersonic Speeds (The Efficiency of Shock
   Diffusers). NACA TM 1140, 1947.

10. Davis, Wallace F., Brajnikoff, George B., Goldstein, David L., and
    Spiegel, Joseph M.: An Experimental Investigation at Supersonic
    Speeds of Annular Duct Inlets Situated in a Region of Appreciable
    Boundary Layer. NACA RM A7G15, 1947.

11. Massachusetts Institute of Technology, Dept. of Elec. Engr. Center
    of Analysis: Tables of Supersonic Flow Around Cones, by Staff
    of Computing Section, Center of Analysis, under direction of
    Zdeněk Kopal, MIT Tech. Rep. No. 1, Cambridge, Mass., 1947.

12. Mangler, W.: Compressible Boundary Layers on Bodies of Revolution.
     MAP, Völkenrode, Repts. and Trans. 47, Mar. 15, 1946.

13. Sibulkin, Merwin: Theoretical and Experimental Investigation of
     Additive Drag.   NACA RM E51B13, 1951.

14. Esenwein, Fred T., and Valerino, Alfred S.: Force and Pressure
     Characteristics for a Series of Nose Inlets at Mach Numbers from
     1.59 to 1.99. I — Conical Spike All—External Compression Inlet
     with Subsonic Cowl Lip. NACA RM E50J26, 1951.

15. Ferri, Antonio, and Nucci, Louis M.: The Origin of Aerodynamic
     Instability of Supersonic Inlets at Subcritical Conditions.
     NACA RM L50K30, 1950.

16. Nucci, Louis M.: The External—Shock Drag of Supersonic Inlets
     Having Subsonic Entrance Flow. NACA RM L50G14a, 1950.

17. Oswatitsch, K. C.: Flows of Compressible Fluids; Fundamental
     Notions and General Theorems. AVA Monographs, A. Betz, ed.
     MAP, Völkenrode, Repts. and Trans. 992, Mar. 15, 1948.

18. Moeckel, W. E.: Approximate Method for Predicting Form and
     Location of Detached Shock Waves Ahead of Plane or Axially
     Symmetric Bodies. NACA TN 1921, 1949.

19. Moeckel, W. E.: Experimental Investigation of Supersonic Flow
     With Detached Shock Waves for Mach Numbers Between 1.8 and 2.9.
     NACA RM E50D05, 1950.

20. Erdmann, S.: Widerstand und Stabilität von Geschosskörpern.
     Lilienthal — Gesellschaft für Luftfahrtforschung, Peenemunde,
     Germany, Bericht 139, Teil 2, Oct. 9—10, 1941, pp. 28—31.

1 Nose inlet model
2 Shroud
3 Floating shell supporting model
4 Stationary shell supporting shroud
5 Strain gage measuring drag force
6 Survey rake
7 Ring and plug for mass flow control
8 Locking screw used during model changes
9 Wedge for outlet area adjustment
10 Mechanism for rotating survey rake
11 Supporting struts
12 Holes for setting angle of attack
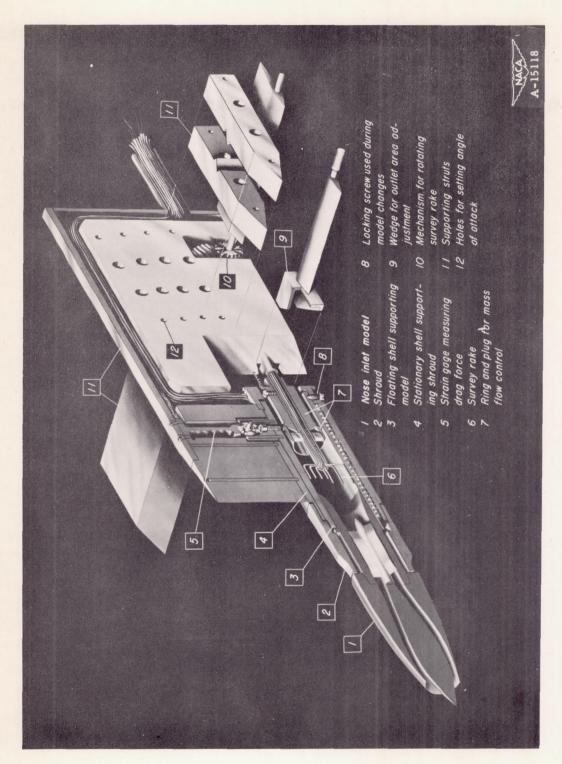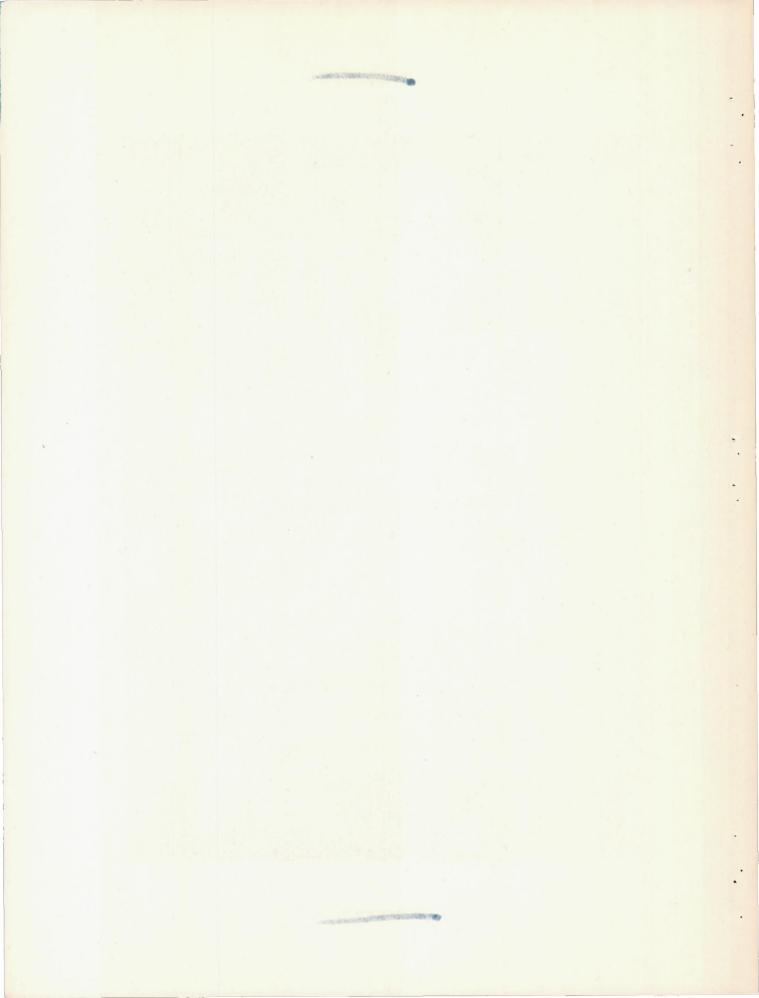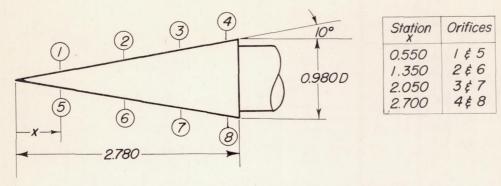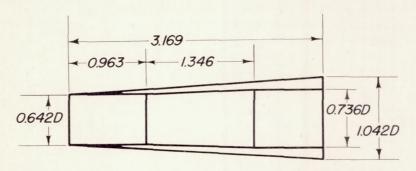
Figure 1.— Apparatus for measuring the performance of supersonic diffusers.
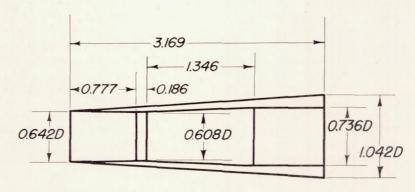
(a) 20° cone with 8 static-pressure orifices.

Station X	Orifices
0.550	1 & 5
1.350	2 & 6
2.050	3 & 7
2.700	4 & 8

(b) Model A.-Open-nose diffuser with a straight inlet section.
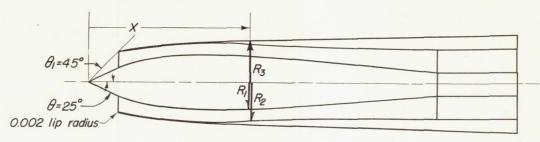
(c) Model B.-Open-nose diffuser with contraction.
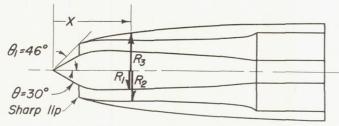
Note: All dimensions are given in inches.

Figure 2.— Model dimensions.

(d)   Model C.— Conical-shock diffuser with internal contraction.

Note: All radii are given normal to model axes.

All dimensions are given in inches.

(e)   Model D.—Conical-shock diffuser without internal contraction.

Model C ordinates

Station X	R_1	R_2	R_3
0	0	—	—
0.322	0.149	0.323	0.323
0.324	0.151	0.321	0.329
0.400	0.184	0.332	0.347
0.500	0.212	0.346	0.363
0.600	0.234	0.361	0.377
0.700	0.252	0.373	0.389
0.800	0.265	0.384	0.400
0.900	0.276	0.393	0.409
1.000	0.284	0.400	0.417
1.100	0.290	0.407	0.423
1.200	0.293	0.413	0.430
1.300	0.294	0.419	0.436
1.400	0.295	0.423	0.440
1.500	0.295	0.427	0.444
1.900	0.273	0.409	0.453
2.400	0.238	0.392	0.466
2.900	0.197	0.380	0.478
3.400	0.153	0.372	0.490
3.702	0.125	0.368	0.498
4.560	0.125	0.368	0.521

Model D ordinates

Station X	R_1	R_2	R_3
0	0	—	—
0.272	0.154	0.282	0.282
0.300	0.167	0.290	0.292
0.350	0.186	0.304	0.310
0.400	0.197	0.312	0.326
0.500	0.211	0.322	0.354
0.575	0.212	0.327	0.367
0.650	0.210	0.329	0.380
0.750	0.207	0.328	0.395
0.850	0.204	0.328	0.408
1.000	0.198	0.326	0.426
1.500	0.176	0.332	0.472
1.900	0.147	0.350	0.497
2.000	0.137	0.360	0.501
2.057	0.125	0.368	0.503
2.500	0.125	0.368	0.518
2.918	0.125	0.368	0.521

Figure 2.- Concluded.
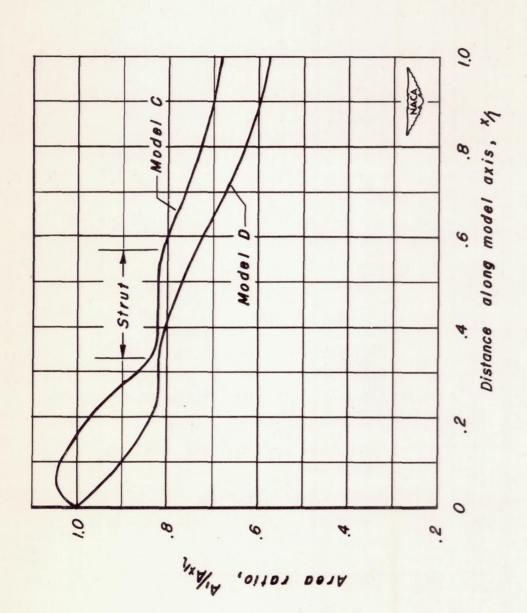
Figure 3.— Variation of diffuser area ratio normal to mean flow direction with diffuser length.
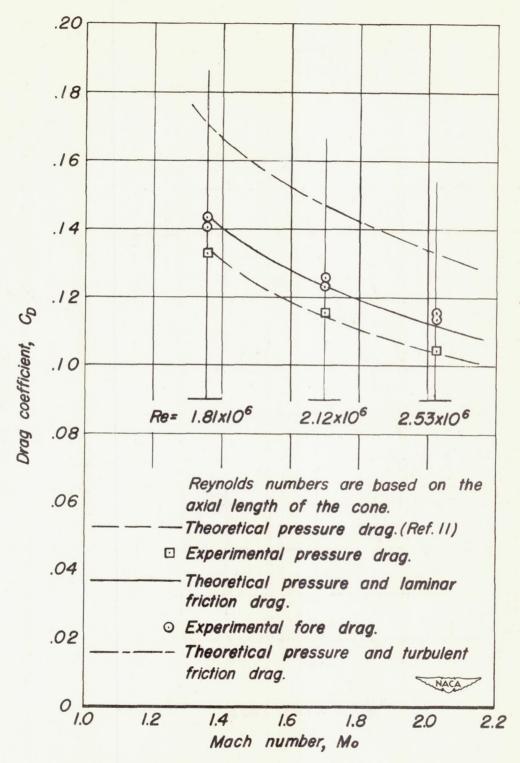
Figure 4.-Fore drag of a 10° semi-angle cone.
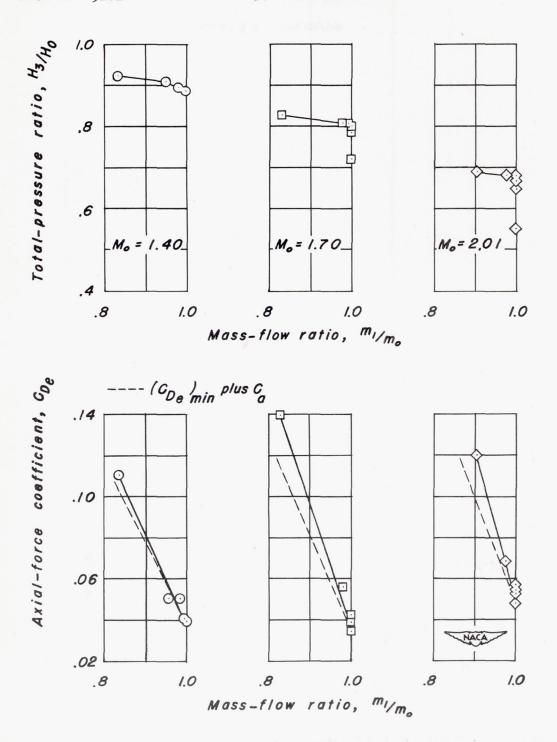
Figure 5.–Variation of total-pressure ratio and axial-force coefficient of model A with mass-flow ratio and Mach number at $\alpha = 0°$.
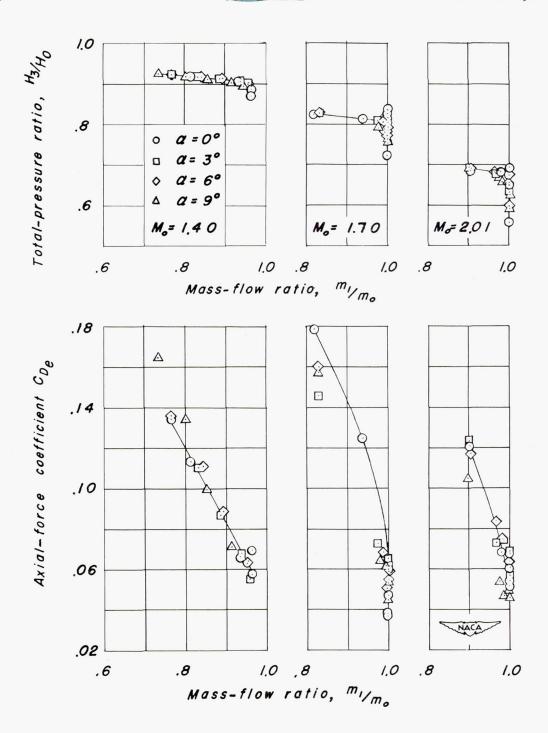
Figure 6.-Variation of total-pressure ratio and axial-force coefficient of model B with mass-flow ratio, angle of attack, and Mach number.
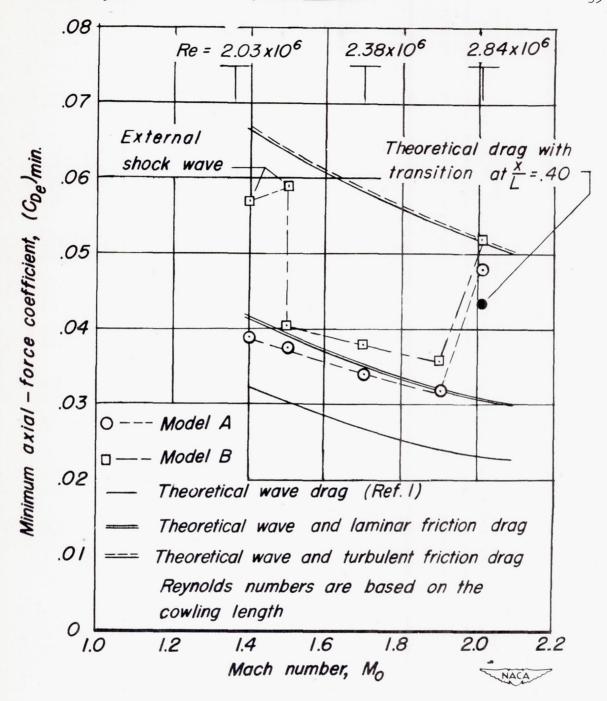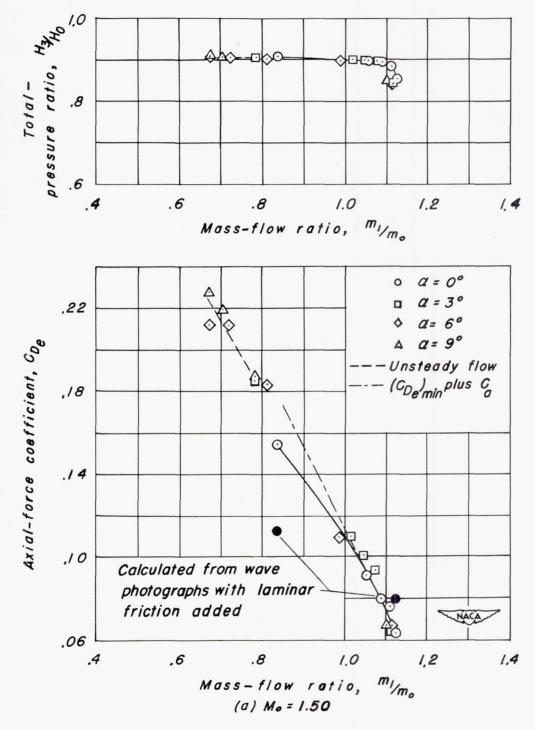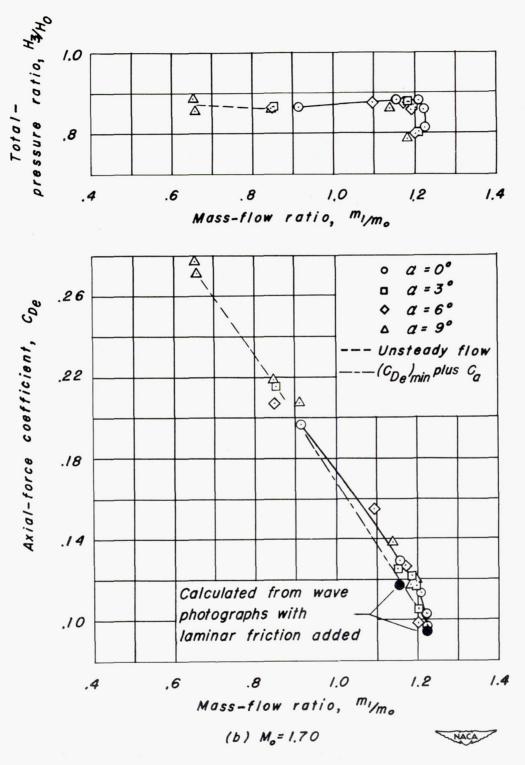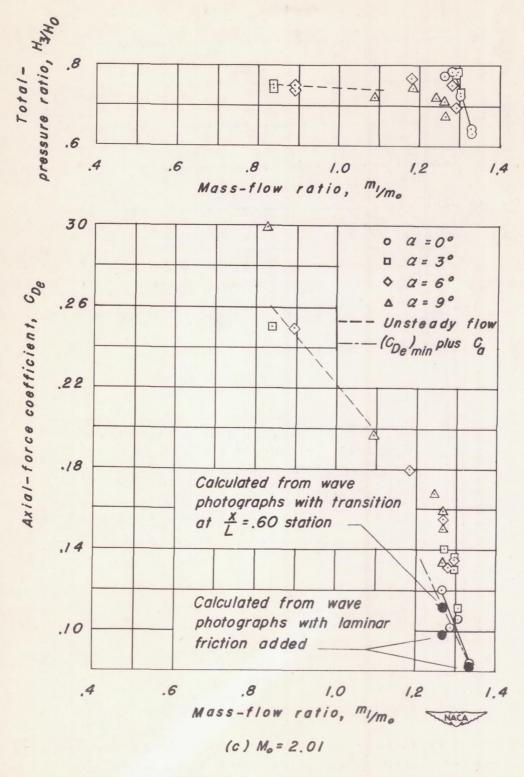
Figure 7. – Variation of the minimum axial-force
coefficient of models A and B with Mach number
at $\alpha = 0°$.

Disturbance due to transition

$M_O = 1.90$ $M_O = 2.01$

NACA
A-15694
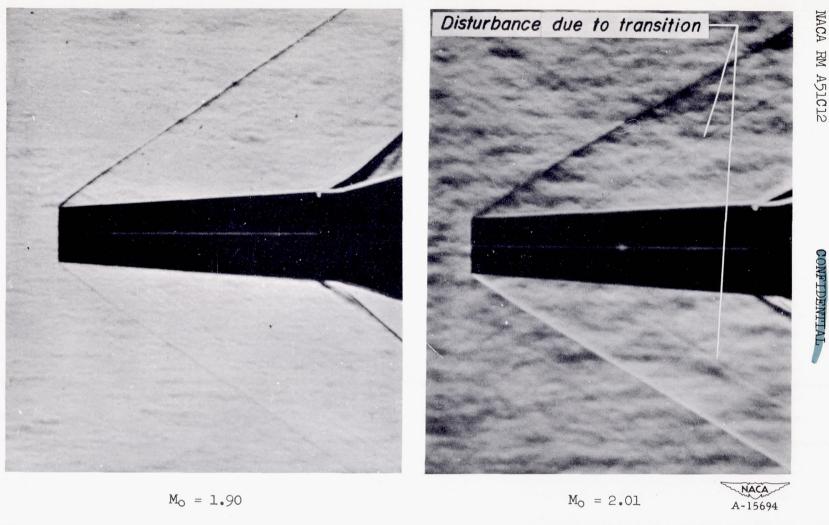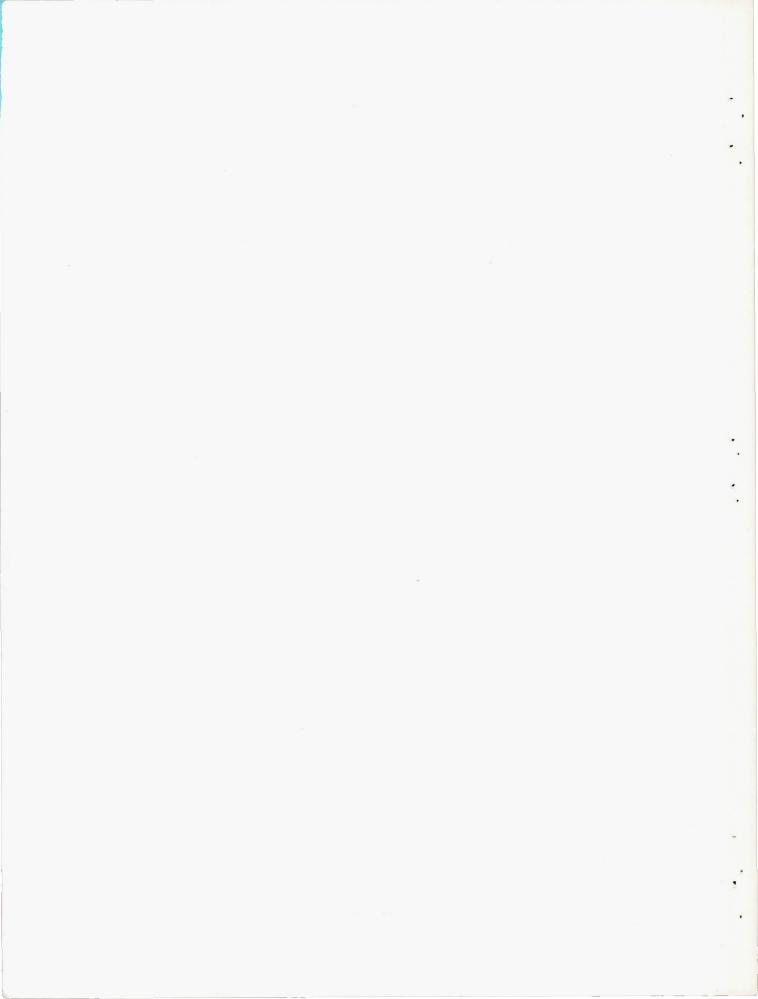
Figure 8.— Typical schlieren photographs of model A showing the pressure distribution due to boundary-layer transition at $M_O = 2.01$.
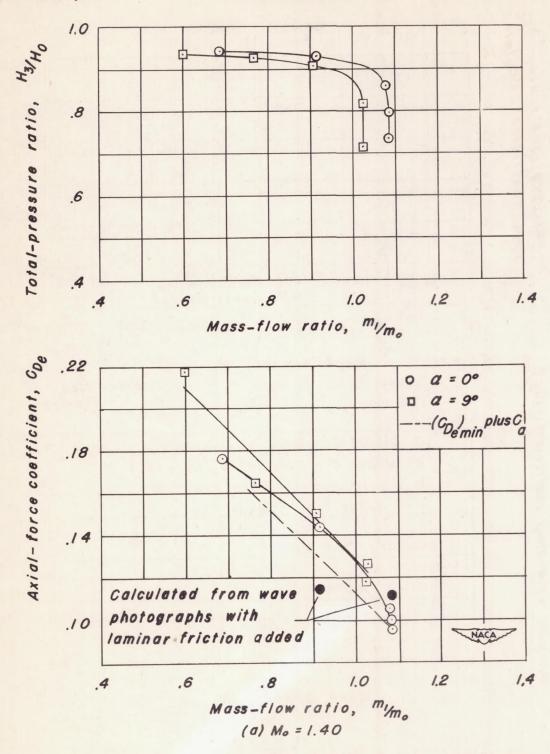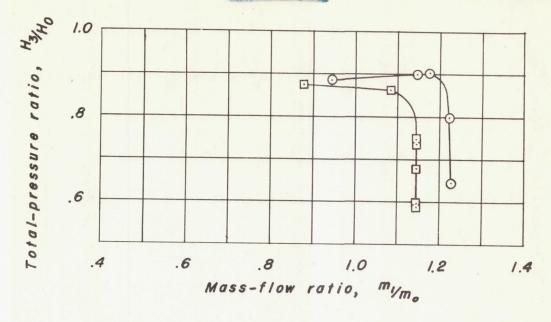
CONFIDENTIAL

Figure 9.— Variation of total-pressure ratio and axial-force coefficient of model C with mass-flow ratio and angle of attack at various Mach numbers.

Total-pressure ratio, H_3/H_0

Mass-flow ratio, m_1/m_0

Axial-force coefficient, C_{De}

$\circ$ $a = 0°$
$\square$ $a = 3°$
$\diamond$ $a = 6°$
$\triangle$ $a = 9°$
---   Unsteady flow
--- $(C_{De})_{min}$ plus C_a

Calculated from wave
photographs with
laminar friction added

Mass-flow ratio, m_1/m_0

(b) $M_0 = 1.70$

Figure 9.— Continued.

(c) $M_o = 2.01$

Figure 9.— Concluded.
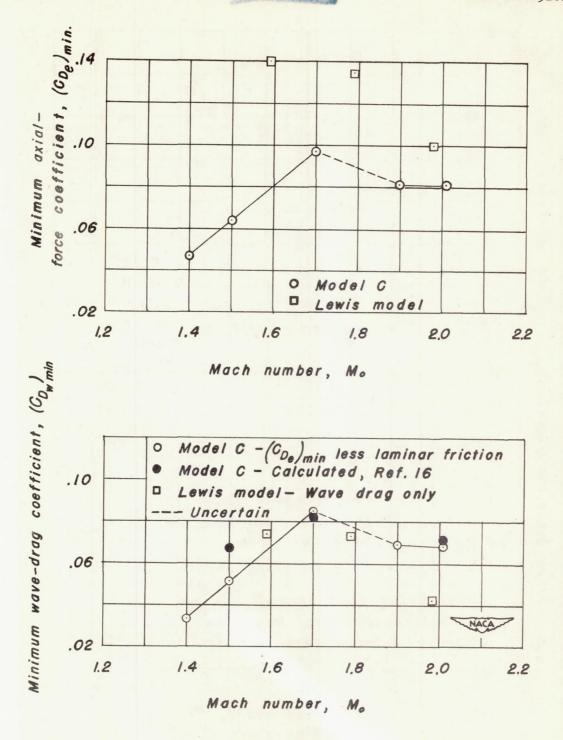
Figure 10.- Variations in minimum axial-force coefficients of model C and Lewis model with Mach number at $\alpha = 0°$.

(a) $M_0 = 1.40$

Figure 11.— Variation of total-pressure ratio and axial-force coefficient of model D with mass-flow ratio and angle of attack at various Mach numbers.
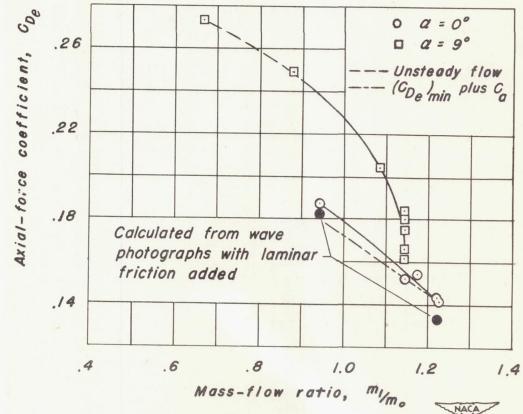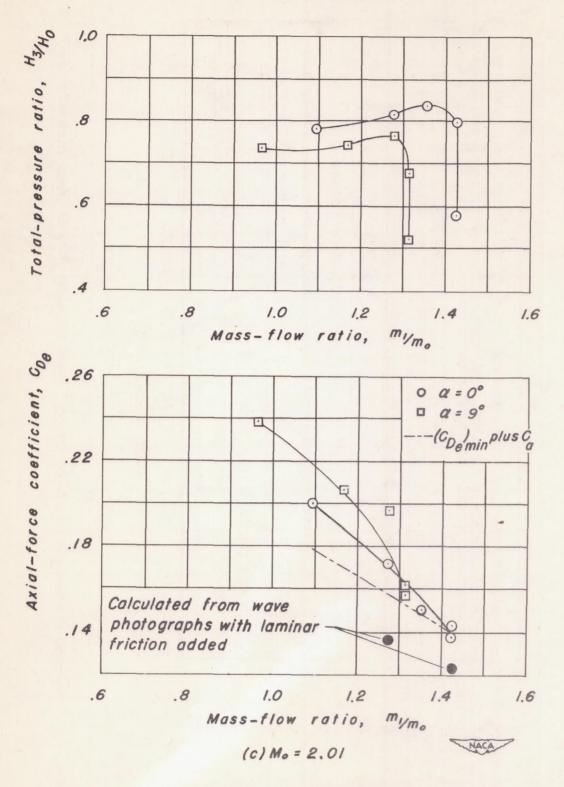
Total-pressure ratio, H_3/H_0 vs Mass-flow ratio, m_1/m_0

$\alpha = 0°$
$\alpha = 9°$
— — — Unsteady flow
— · — $(C_{De})_{min}$ plus C_a

Calculated from wave photographs with laminar friction added

Axial-force coefficient, C_{De} vs Mass-flow ratio, m_1/m_0

(b) $M_0 = 1.70$

Figure 11.— Continued.

(c) $M_0 = 2.01$

Figure 11.- Concluded.
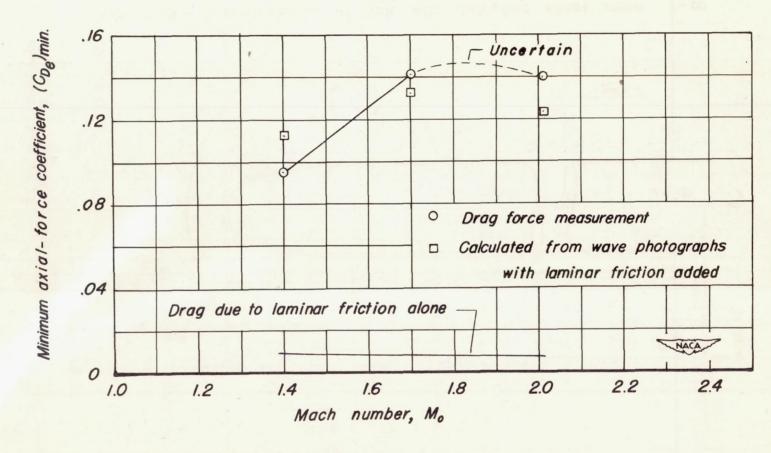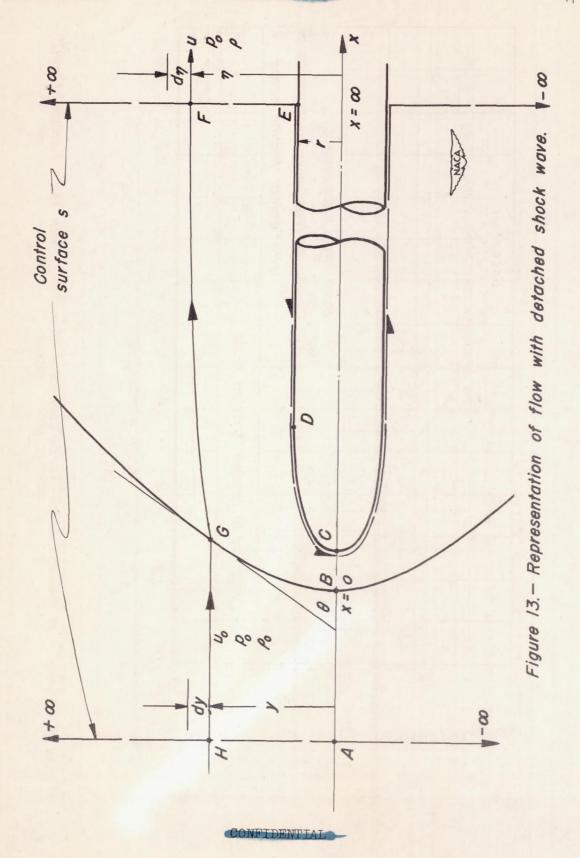
Figure 12.—Variation of minimum axial-force coefficient of model D with Mach number at $\alpha = 0°$.
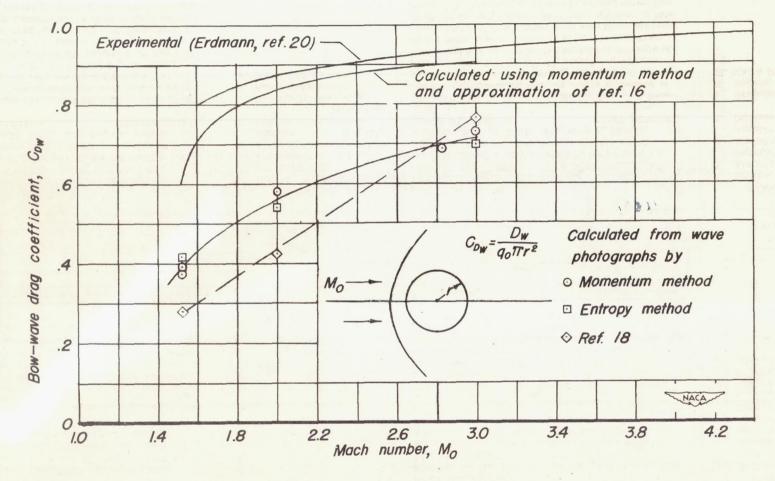
Figure 13.— Representation of flow with detached shock wave.

Figure 14.–Comparison of calculated and experimental values of the bow-wave drag of a sphere at various Mach numbers.

52-11